

1 Whole-cell modeling in yeast predicts compartment-specific

2 proteome constraints that drive metabolic strategies

3

4 Ibrahim E. Elsemman^{1,7,#}, Angelica Rodrigues Prado^{2,3,#}, Pranas Grigaitis^{2,#}, Manuel Garcia

5 Albornoz⁴, Victoria Harman⁵, Stephen Holman⁵, Johan van Heerden², Frank J. Bruggeman², Mark

6 M.M. Bisschops³, Nikolaus Sonnenschein¹, Simon Hubbard⁴, Rob Beynon⁵, Pascale Daran-

7 Lapujade³, Jens Nielsen^{1,6,*}, and Bas Teusink^{2,*}

8

9 ¹ Novo Nordisk Foundation Center for Biosustainability, Technical University of Denmark,
10 DK2800 Lyngby, Denmark

11 ² Systems Biology Lab, Amsterdam Institute of Molecular and Life Sciences, Vrije Universiteit
12 Amsterdam, The Netherlands

13 ³ Department of Industrial Microbiology, Technical University Delft, Delft, The Netherlands

14 ⁴ Division of Evolution & Genomic Sciences, University of Manchester, Manchester, UK

15 ⁵ Institute of Systems, Molecular and Integrative Biology, University of Liverpool, Liverpool, UK

16 ⁶ Department of Biology and Biological Engineering, Chalmers University of Technology,
17 SE41296 Gothenburg, Sweden

18 ⁷ Current address: Department of Mathematics, Faculty of Science, Assiut University, Assiut,
19 Egypt

20

21 # These authors contributed equally to this work

22 * To whom correspondence should be addressed: nielsenj@chalmers.se (JN), b.teusink@vu.nl

23 (BT)

24 Abstract

25 **When conditions change, unicellular organisms rewire their metabolism to sustain cell**
26 **maintenance and cellular growth. Such rewiring may be understood as resource re-allocation**
27 **under cellular constraints. Eukaryal cells contain metabolically active organelles such as**
28 **mitochondria, competing for cytosolic space and resources, and the nature of the relevant cellular**
29 **constraints remain to be determined for such cells. Here we developed a comprehensive metabolic**
30 **model of the yeast cell, based on its full metabolic reaction network extended with protein**
31 **synthesis and degradation reactions (16304 reactions in total). The model predicts metabolic**
32 **fluxes and corresponding protein expression by constraining compartment-specific protein pools**
33 **and maximising growth rate. Comparing model predictions with quantitative experimental data**
34 **revealed that under glucose limitation, a mitochondrial constraint limits growth at the onset of**
35 **ethanol formation - known as the Crabtree effect. Under sugar excess, however, a constraint on**
36 **total cytosolic volume dictates overflow metabolism. Our comprehensive model thus identifies**
37 **condition-dependent and compartment-specific constraints that can explain metabolic strategies**
38 **and protein expression profiles from growth rate optimization, providing a framework to**
39 **understand metabolic adaptation in eukaryal cells.**

40 Macromolecular synthesis and energy conservation by metabolism underlies cellular
41 maintenance, growth and fitness. Unicellular organisms such as yeasts generally display a great
42 variety of metabolic strategies that lead to competitive fitness across conditions¹. The associated
43 reprogramming of metabolism between such metabolic strategies is of key interest in
44 biotechnology and biomedical research.

45 One well-known example is “overflow” metabolism, in which under aerobic conditions
46 not all substrate is fully oxidized but secreted as by-products. In cancer cells it is referred to as
47 the Warburg effect: enhanced glycolytic activity with lactate as byproduct at the expense of
48 respiration². The same phenomenon is known as the Crabtree effect in *Saccharomyces*
49 *cerevisiae* (Baker’s yeast)³. At sugar limitation, in the presence of oxygen, yeast respire glucose
50 completely to CO₂ for ATP generation; at sugar excess, it displays respirofermentative
51 metabolism, where respiration is combined with ethanol formation (alcoholic fermentation).
52 The extent to which these two metabolic strategies are used can be titrated in a glucose-limited
53 chemostat: at a specific, “critical”, dilution (=growth) rate, ethanol formation starts and
54 increases linearly with growth rate⁴. Other microorganisms show similar behaviour⁵: for
55 example, *E. coli* produces acetate at higher growth rates at the expense of respiration⁶.

56 In the last decade, a theoretical framework has been developed that can explain why
57 cells shift metabolic strategies upon environmental or gene-expression perturbations^{5,7-10}. It is
58 essentially based on the catalytic benefits of proteins, and their associated costs¹¹. These costs
59 comprise competition for building blocks, energy and synthesis machineries; and for space in
60 cellular compartments. Two key features of this resource allocation paradigm can explain
61 metabolic adaptations. First, cellular compartments are or can become “full”, which is the case
62 when they are fully occupied with (maximally) active proteins, and an increase in one protein
63 has to come at the expense of another. This was postulated as a phenomenological rule based on
64 experimental observations¹², but also follows naturally from growth-rate maximization¹³: at the
65 maximum growth rate that is attainable at any condition, at least one compartment must be fully
66 occupied and thus actively limit that growth rate. Second, cells allocate their limited resources

67 for protein synthesis according to their demands^{14,15}. Consequently, fractions of needed proteins
68 vary with growth rate within compartments whose protein content is bounded, and this can lead
69 to “active proteome constraints” related to full compartments.

70 Within this framework, the onset of overflow metabolism was explained by the smaller
71 protein cost of generating ATP through fermentation than respiratory pathways^{6,7}; this becomes
72 important under fast growth, when biosynthesis and ribosome demands are high and thus
73 require large proteome fractions. Earlier work suggests that the proteome-constrained resource
74 allocation paradigm, which was largely developed for *E. coli*, may also be a powerful perspective
75 for regulation of eukaryal yeast metabolism, such as ribosome biosynthesis¹⁶, and growth on
76 different sugars¹⁷. However, a key feature of the metabolism of a eukaryal cell is the presence of
77 metabolically active organelles, most prominently mitochondria. Each organelle introduces two
78 new compartments (intra-organelle space and membrane), and how these compartments
79 impacts adaptation of metabolism, and which compartments become limiting under different
80 conditions, is an open question.

81 Moreover, despite the wealth of experimental data on *Saccharomyces cerevisiae*, a
82 comprehensive, quantitative, data set in which growth rate is systematically varied and both
83 fluxes and protein expression levels are measured, which are needed to validate resource
84 allocation predictions, are still rare (see however, some recent studies^{16,18}).

85 Here we generated such high-quality comprehensive data sets, and in parallel developed
86 the most detailed and comprehensive, compartmentalized and quantitative model of metabolism
87 and protein synthesis of yeast. The model can compute the costs and benefits of protein
88 expression and translocation; It can be used to interpret or predict experimentally determined
89 changes in growth rate, protein expression and metabolic fluxes as a result of growth rate
90 optimization through resource allocation into different, compartmentalized, proteome fractions.
91 Comparison of the model predictions with the data gives unprecedented insight into our
92 physiological understanding of this important model organism.

93

94 Results

95 Construction of a comprehensive proteome-constrained yeast model

96 We extended an existing¹⁹ metabolic genome-scale metabolic model of yeast (GEM), by
97 coupling metabolic fluxes to the synthesis of the catalysing enzyme and added constraints on
98 protein concentrations, expressed as protein fractions of the total proteome (Fig. 1a). We refer
99 to the resulting model as proteome-constrained Yeast (pcYeast). Earlier GEM-based approaches
100 exist that incorporate resource allocation, and for yeast, these considered constraints on enzyme
101 activities and total protein content^{17,20–23}, whereas for *E. coli* there were added constraints and
102 reactions associated with transcription and translation⁹. Others considered membrane-area
103 constraints and limitations of protein allocation to specific pathways^{8,24}. We combined all these
104 extensions (see Supplementary Notes for detailed information) to make pcYeast: a next-
105 generation yeast GEM and computable knowledge base that incorporates protein expression,
106 translation, folding, translocation and degradation at genome-scale for a compartmentalized,
107 eukaryal, organism. In our current model, we consider the protein compartments most relevant
108 for central metabolism: plasma membrane, cytosol, mitochondrion, and mitochondrial
109 membrane. Other cell compartments such as the nucleus or endoplasmic reticulum are not (yet)
110 specified explicitly - but do occupy volume in the cytosol.

111 The cellular proteome was divided into metabolically active, ribosomal, and unspecified
112 (UP) proteins. The UP fraction is cytosolic, has an average amino acid composition and is added
113 to always maintain a constant protein density in the cytosol. It has a minimum expression level
114 estimated from the experimental proteomics data (Supplementary Notes). The minimal UP
115 fraction represents growth-rate independent structural, signalling and “household” proteins.
116 Higher expression of UP than minimal represent both unspecified anticipatory proteins, or
117 metabolic proteins that do not carry flux – including the unsaturated fraction of flux-carrying
118 enzymes.

119 Metabolic enzymes are assigned to a specific compartment, either cytosol, plasma
120 membrane, mitochondrial matrix or inner mitochondrial membrane; Mitochondrial proteins
121 require additional protein transport complexes²⁵. For each protein, we comprehensively
122 modelled synthesis and degradation processes, which are responsible for the largest fraction of
123 cellular energy usage. Our model includes 1,523 proteins, whose life cycles are described by
124 16,304 reactions that include translation initiation, elongation and termination factors,
125 ribosomal assembly factors, protein-specific folding by chaperones and degradation reactions,
126 as well as 5'UTR-length dependent energetic costs for translation initiation ([Table 1](#),
127 [Supplementary Notes](#)).

128 We applied three classes of constraints that couple metabolic fluxes and peptides
129 synthesis rates ([Fig. 1b](#) and [Supplementary Notes](#) for details). The *enzyme capacity constraint*
130 sets the minimal enzyme synthesis rate required to achieve a certain metabolic flux. Thus, all
131 metabolically-active proteins are modeled to work at their maximal rate and are minimally
132 expressed; the unspecified protein was used to maintain protein density. In this way we prevent
133 choices about unknown regulatory and kinetic mechanisms that may affect the activity of
134 enzymes; rather we use the deviation between predicted minimal and measured actual protein
135 expression levels to indicate such effects. The total enzyme synthesis rate is constrained by the
136 abundance of ribosomes through a *ribosome capacity constraint*, for both cytosol and
137 mitochondria. Finally, we added *compartment-specific constraints* on the proteome, for the
138 cytosol, the plasma membrane, and the mitochondrial matrix and inner membrane, ([Fig. 1b](#)).
139 The values for these constraints are based on independent literature data or were fitted to
140 experimental data (as explicated in [Supplementary Notes](#)) and the values are either fixed or
141 growth-rate dependent, depending on the nature of the constraint.

142 The steady-state metabolite balances, the enzyme synthesis and degradation balances,
143 and the compartment-specific proteome constraints together specify a linear program with its
144 fluxes as optimisation variables, provided the growth rate is treated as a parameter. We use a
145 binary search algorithm to find the maximum growth rate where the linear programming

146 problem becomes just infeasible; the model returns all the flux values associated with the
147 maximal feasible growth rate.

148

149 [Calibrating the model against experimental data](#)

150 We performed a series of experiments for collection of high-quality datasets of fluxes
151 and protein levels, used either as model input or for comparison with model predictions. We
152 used glucose-limited continuous cultures operated at dilution rates close to the critical dilution
153 rate for ethanol formation, to capture proteome change upon the onset of overflow metabolism.
154 Additionally, we varied the growth rate in pH-controlled batch experiments, either with
155 different sugar quality or through translation inhibition. We measured fluxes, including O₂ and
156 CO₂ fluxes ([Supplementary Dataset 1](#)), which combined with biomass measurements, allowed to
157 estimate the so-called maintenance parameters, i.e. ATP usage that is not explicitly accounted for
158 in the model ([Supplementary Notes](#)). Label-free proteome quantification allowed us to reliably
159 estimate proteome fractions of around 3000 of the 6000 proteins ([Supplementary Datasets 2, 3,](#)
160 [and 4](#)).

161 Parameters associated with translation strongly affected our model outcomes, and we
162 used published quantitative proteomics data¹⁶ to estimate parameters for protein translation,
163 such as the elongation rate ([Supplementary Notes](#)). According with experimental reports we
164 assumed a constant inactive fraction of ribosomes, and a fixed saturation of the actively
165 translating ribosomes^{16,27} and were hereby able to describe the growth-rate dependent
166 ribosome mass fraction with the model ([Fig. 1c](#)). As evidence for correctly capturing the costs of
167 protein synthesis, we correctly predicted the effect of over-expressing mCherry, an unneeded,
168 “gratuitous” protein, on the specific growth rate ([Fig. 1d](#)).

169

170 [The model predicts shifts in metabolic strategies](#)

171 We subsequently used the model to analyse yeast’s physiological response to different
172 levels of glucose availability. Traditional Flux Balance Analysis computes continuous chemostat

173 cultures by minimizing glucose uptake rate at fixed growth (=dilution) rate²⁸. Here we
174 simulated glucose availability by varying the degree of saturation of the glucose transporter. We
175 needed to constrain the maximal expression level of the glucose transport system, based on
176 literature data (Supplementary Notes), as leaving expression free to occupy available membrane
177 space led to unrealistically high expression levels and overestimation of growth rate at
178 subsaturating glucose levels. We subsequently computed the maximal feasible growth rate and
179 compared model predictions with published data²⁹, and from our glucose-limited chemostat
180 cultures (growth rates between 0.2 – 0.34 h⁻¹). We also included our data from batch cultures on
181 glucose (growth rates 0.37-0.39 h⁻¹) and on trehalose; Trehalose is a disaccharide of two glucose
182 molecules, hydrolyzed extracellularly³⁰, thus providing slow release of glucose that supports low
183 growth rates.

184 The maximal feasible growth rate that the model predicted can be linked directly to the
185 dilution rate in the chemostat, allowing comparison of model prediction and data (Fig. 2a). The
186 (residual) glucose concentrations were calculated from documented (high) affinity of the
187 transporters, which is close to 1 mM³¹. The resulting relationship between growth rate and
188 residual glucose concentration fit experimental data very well (Fig. 2b), validating our
189 expectation that we could ignore intracellular glucose³². Predicted biomass yield (Fig. 2c) and
190 fluxes (Fig. 2d) corresponded well with the experimental data, as did the intracellular flux ratios
191 from previously published ¹³C-labeling flux analysis at three specific growth rates in glucose-
192 limited chemostat cultures (Supplementary Figure 1). In particular, the model predicted a
193 maximal oxygen consumption rate at dilution rates higher than 0.28 h⁻¹, at the onset of ethanol
194 formation. Above 0.35 h⁻¹, this rate rapidly drops to the low level that is observed under glucose
195 excess (batch) conditions. We conclude that the model can adequately predict the changes in
196 metabolic fluxes when the growth rate is varied through the availability of glucose.

197

198 Changes in metabolic strategies are the result of proteome constraints

199 We used pcYeast to identify the active proteome constraints, *i.e.* the protein pools that
200 limit growth rate, because, according to resource allocation theory, the number of active
201 proteome constraints determines the maximal number of independent metabolic behaviors that
202 are possible in optimal states^{5,13}. For this we computed the occupancy of each protein pool: a
203 pool that is fully occupied is indicative of an active constraint. At low growth rates, below 0.28 h⁻¹,
204 the glucose transporter is the only proteome pool that is fully occupied (Fig 2e). With only
205 glucose uptake as active constraint, pure respiration is the single optimal strategy. At the onset
206 of ethanol formation, a second metabolic mode started to carry flux (for formal computation of
207 these modes and the concomitant theory, see Supplementary Notes), and thus a second
208 constraint must have become active. Indeed, at this growth rate the occupancy of the inner-
209 mitochondrial membrane became maximal (Fig. 2e). Thus, the model suggests that under
210 glucose-limited chemostat conditions, the onset of ethanol formation is caused by a limit of the
211 mitochondrial membrane space, and hence the amount of proteins that yeast can maximally
212 express in this compartment.

213 At a growth rate of 0.35 h⁻¹ we found that the unspecified protein level reached its
214 minimal value (Fig. 2e), equivalent to the cytosol being completely filled with maximally active
215 proteins. Further growth rate increase requires higher ribosomes and biosynthetic protein
216 fractions, which now has to come at the expense of the least proteome efficient pathway. The
217 model confirmed earlier calculations³³ that respiration is less proteome efficient than
218 fermentation (Supplementary Figure 2) and respiration is therefore replaced by fermentation.
219 The model suggested therefore that at growth rate above 0.35 h⁻¹ the second growth-limiting
220 constraint was shifted from the mitochondrial proteome to the cytosolic proteome. Thus, the
221 metabolic changes in the model, when growth rate and thus metabolic fluxes increase, are
222 dictated by the filling up of different cellular compartments with active protein, unique for an
223 eukaryal cell. The level of detail in our model to identify the condition-dependent, active,

224 protein-concentration constraints belonging to different compartments has so far not been
225 provided by any other model.

226

227 [Proteomics data validates model predictions](#)

228 We subsequently measured protein levels with quantitative proteomics and compared
229 them to the model predictions. We expected to underestimate most proteome fractions, because
230 the model predict minimal protein levels required to support metabolic flux. Especially at lower
231 growth rates where nutrient limitation is most severe, one can expect lower average enzyme
232 saturation, and indeed we observed larger deviations between predicted minimal protein levels
233 and measured protein fractions at low growth rates ([Fig. 3a](#)). The difference between the
234 predicted minimal level and the data may be interpreted as a proxy for the average saturation of
235 enzymes. We see an overall tendency that the saturation of enzymes increases with growth rate
236 ([Supplementary Figure 3](#)). This is most prominent for the glycolytic pathway; also for amino
237 acid biosynthesis, the protein expression is higher than expected based on metabolic activity,
238 indicating also here a substantial undersaturation of the enzymes, as observed before for
239 bacteria such as *E. coli*³⁴ and *L. lactis*³⁵. We find similar patterns for other biosynthetic pathways,
240 except for lipids ([Supplementary Figure 4](#)).

241 For mitochondrial proteins involved in the citric acid cycle and respiration, however, we
242 found that predicted minimal proteome fractions were very close to the measured ones ([Fig.](#)
243 [3a](#)). Unless *kcats* of mitochondrial enzymes are systematically underestimated, this indicates
244 that mitochondrial proteins work at higher average saturation than cytosolic proteins - and
245 seemingly close to their maximal capacity. Regardless of absolute numbers, the saturation of the
246 mitochondria seems rather constant, suggesting that yeast tunes the total amount of
247 mitochondria, rather than make excess (but subsaturated) mitochondria, at least under these
248 conditions. This may make sense, given the extra costs of mitochondrial components such as
249 membranes, and for protein translocation of host-derived proteins during mitochondrial
250 biogenesis, which competes for membrane space with respiratory proteins.

251 Upon closer inspection, we observed that at the onset of ethanol formation the total
252 mitochondrial protein fraction started to decrease (Fig. 3b). The observed decay follows the
253 theoretical dilution-by-growth kinetics if at that point the rate of mitochondrial biosynthesis has
254 reached a maximum (Fig. 3b). Thus, the data suggests that the rate of mitochondrial biogenesis,
255 rather than the maximal mitochondrial membrane area currently used by the model, may reach
256 the host's maximal capacity at the onset of ethanol formation. When we zoom in on the
257 mitochondrial proteome, we find that the mitochondrial ribosome fraction increased as a
258 function of growth rate, and also other proteins re-allocated (Supplementary Fig. 5). Indeed,
259 mitochondria are self-replicating entities abiding to the same resource allocation principles as
260 the host, which even includes selection for fast replication - but obviously severely dictated by
261 the proteins the host provides. More data related to the mitochondrial biosynthetic processes,
262 such as mitochondrial ribosomal capacity and protein import machinery would be required to
263 predict the maximal mitochondrial growth rate from first principles, which is outside the scope
264 of this study. Nonetheless, the distinct changes of mitochondrial proteins at the critical dilution
265 rate are consistent with the model prediction that a mitochondrial constraint is responsible for
266 the onset of ethanol formation under glucose-limited conditions.

267

268 Constraints and fluxes under sugar excess conditions

269 We then varied growth rate (between 0.05 h^{-1} and 0.4 h^{-1}) by providing different sugars,
270 i.e. trehalose, galactose, maltose and glucose during batch cultivation. Ethanol production was
271 already observed on galactose, already at a growth rate of 0.16 h^{-1} so at a much lower growth
272 rate than the critical growth rate of 0.28 h^{-1} under glucose-limited growth (Fig. 4a). Maltose
273 showed intermediate growth rate and fluxes. Initial model simulations with a "naïve" model
274 using the reported catalytic rates of the transporters and catabolic enzymes involved in
275 galactose and maltose metabolism, however, resulted in predicted growth rates and fluxes not
276 far from growth on glucose. This suggests that there are additional cost factors that were not

277 included in the model, and or that *Saccharomyces cerevisiae* is not as well adapted to these
278 sugars.

279 We therefore used the model as data analysis tool to estimate possible changes in
280 parameters that fit the observed growth rate and corresponding fluxes (see [Supplementary](#)
281 [Notes](#) for details). Such parameter changes may be interpreted as costs for suboptimal
282 metabolism of carbon sources other than glucose. The onset of ethanol formation at a growth
283 rate of 0.16 h^{-1} required a combination of changes in both sugar uptake and the intracellular
284 proteome (through the minimal UP fraction constraint): a lower sugar uptake capacity alone
285 would be identical to lowering saturation of the transporter as was done for glucose ([Fig 2](#)), and
286 pure respiration would have been found at 0.16 h^{-1} . Conversely, only an increase in minimal UP
287 would have resulted in a proportional flux decrease that we also found with mCherry
288 overexpression (or translation inhibition, [Supplementary Figure 6](#)), and more ethanol were to
289 be found.

290 We had to decrease the maximal galactose uptake rate by a factor of 2.5 compared to
291 glucose. Furthermore, an increase in minimal UP fraction was needed, to 0.49 g/g protein . To fit
292 all fluxes optimally, we also required additional energetic costs (see [Supplementary Notes](#)),
293 whose mechanistic underpinning remains to be explored but may be related to the reported
294 toxicity of galactose intermediates³⁶. Such a change in energetic costs were not needed to
295 describe the data for growth on maltose: only a change in the maltose uptake rate and minimal
296 UP fraction (of 0.34 g/g protein) were required to achieve good fit.

297 For maltose, a disaccharide of glucose, the reason for the required parameter changes is
298 not clear. Only a maltose proton-symporter and a maltase protein distinguishes it from growth
299 on glucose. The transport expression may be tightly regulated as very high maltose uptake rates
300 can result in substrate-accelerated death³⁷. For galactose, the toxicity of its intermediates³⁶
301 results in an evolutionary trade-off with growth on glucose³⁸; on galactose yeast cells appear to
302 be still prepared for growth on glucose, which may prevent them from optimal expression of
303 proteins on galactose, as shown by expression titration experiments³⁹. Indeed, laboratory

304 evolution experiments on galactose select mutations in Ras/cAMP signalling and adapted strains
305 show increased growth rates and concomitant increased ethanol fluxes³⁸. Interestingly, the
306 direction of change points to the optimal behaviour predicted by the initial naïve model,
307 suggesting that the pcYeast model may aid in predicting the direction of evolutionary change
308 during laboratory evolution experiments ([Supplementary Figure 7](#)).

309 With the updated parameters, we identified for both sugars that the active constraints
310 limiting growth were the sugar transport expression and the minimal UP fraction constraint
311 ([Figure 4d, Supplementary Notes, Supplementary Figure 8](#)). These active constraints explains
312 ethanol formation during growth on galactose even though the growth rate is lower than the
313 critical dilution rate on glucose.

314

315 [Proteomics data on sugar excess shows re-allocation of metabolic strategies](#)

316 If growth rate is actively constrained by the cytosolic proteome under galactose, maltose
317 and glucose excess conditions, it implies that all cytosolic proteins work at their maximum
318 activity, and changes in flux must be brought about by changes in protein level. We therefore
319 turned to proteomics again. Comparing the minimal levels of the model with experimental data,
320 we find again that mitochondrial proteins for the TCA cycle and respiration are very similar to
321 the predicted minimal levels required to sustain flux ([Fig. 4c](#)). Cytosolic proteins were
322 underestimated - even at sugar excess conditions. (Note however that the expected maximal
323 attainable activity is not likely at the maximal rate in the forward direction as product inhibition
324 is inevitable in a chain of enzymes.)

325 More indicative of “a full cytosol” is that at the onset of ethanol formation (at galactose
326 growth rate and higher) we find evidence for proportional relationships between protein and
327 flux for high-flux carrying, pathway-grouped, proteins as a function of growth rate ([Fig. 4c](#)). This
328 is observed even down to the individual protein level, as illustrated for glycolytic and
329 respiratory proteins in [Fig. 4d](#). This implies that under these conditions, enzyme saturation was
330 constant (and maximal, we expect) and changes in flux could only be brought about by

331 corresponding changes in enzyme levels. This data illustrates how mitochondrial proteins are
332 being traded in for glycolytic proteins needed for an enhanced fermentation and growth rate. It
333 also confirms the model's prediction that the cytosolic proteome constraint is active during
334 growth on these sugars.

335
336 [Inhibition of translation highlights the role of environmental signaling in coordination](#)
337 [of metabolism in yeast.](#)

338 Finally we varied growth rate by translation inhibition by cyclohexamide under
339 controlled glucose batch conditions, and again measured fluxes, growth rate and proteome
340 profiles ([Fig. 5a](#)). Upon inhibition of translation, we found a decrease in growth rate and close to
341 proportional decreases in glucose, ethanol and CO₂ fluxes, for both the model and the
342 experimental data ([Fig. 5b](#)). Such behaviour is expected when one dominant constraint is active
343 and its extent is varied (cf. glucose-limited fully respiratory growth, [Fig. 2](#)). In the case of glucose
344 excess, the model suggested that the cytoplasmic volume was fully occupied with active proteins
345 (minimal UP constraint was hit), and inhibition of translation required higher expression levels
346 of ribosomes, taking away limited proteome space for growth-supporting activities.

347 However, experimental observations compromised this initial explanation. First, for
348 oxygen the model also predicted a proportional increase with growth rate, but experimentally
349 the fluxes did not change much as did the expression of enzymes involved in oxygen
350 consumption, such as TCA cycle and oxidative phosphorylation ([Fig. 5d](#)). Moreover, the
351 ribosomal proteome fraction increased much less with inhibition than the model predicted ([Fig.](#)
352 [5c](#)). Since translation inhibition in the model has the same effect as overexpression of a non-
353 functional protein ([Supplementary Figure 6](#)), we followed the earlier observation that the
354 inactive fraction of ribosomes could be recruited for translation, depending on the translational
355 load¹⁶, with only a small improvement ([Supplementary Figure 9](#)).

356 This suggested that either some constraint prevents the ribosomal fraction from
357 increasing to the optimal levels predicted by the model, or the expression of ribosomes in yeast

358 is dominantly regulated by environmental nutrient signalling and less by internal cues. A
359 dominant role of signalling in ribosomal biogenesis has been suggested before¹⁶. In yeast the
360 TOR pathway appears to be the master regulator of ribosomal biosynthesis and assembly at
361 steady-state growth^{40,41}. Following the TOR-specific targets described by Kunkel⁴¹, we find that
362 key target proteins of this signalling pathway, including ribosomal auxiliary factors, had
363 constant expression levels (**Supplementary Figure 10 and Supplementary Table 1**), supporting
364 the dominant role of external rather than internal cues.

365 When we constrained ribosomal expression to the measured maximal response,
366 ribosomal expression rapidly became the only active constraint in the model, and the proteome
367 space that became available in the cytosol at the lower growth rates was used for increased
368 respiration (**Supplementary Figure 10**). This is not observed experimentally, and our data
369 suggest that respiration does not respond to internal cues either. In contrast the fluxes and
370 expression of proteins involved in glycolysis and amino acid metabolism did decrease with
371 growth rate (**Fig. 5bd**). This suggests that these pathways must be sensitive to internal feedback
372 regulation, as is well known for amino acid metabolism⁴². Thus, the proportional fluxes we found
373 for ethanol and glucose upon translation inhibition, are likely the result of control by demand⁴³,
374 with lower demand at lower growth rate.

375

376 Discussion

377 In this work, we developed the most comprehensive model of a growing,
378 compartmentalized, eukaryal cell to date. It includes all its known metabolic reactions, and
379 details of the protein synthesis, degradation and transport machinery to express the enzymes.
380 The key of our approach is the application of constraints on protein pools in the different
381 compartments that have direct biochemical meaning and could be independently estimated
382 from literature data. Our approach is unique in level of detail and in dealing with cellular
383 compartmentation, in particular of the mitochondria. We furthermore generated a unique set of

384 high-quality quantitative data on both fluxes and the proteome under different, well-controlled,
385 conditions. Through integration and comparison with the model, we provide deeper insight into
386 the physiology of *Saccharomyces cerevisiae*.

387 First, we firmly established that metabolic growth strategies of yeast on glucose can be
388 well understood from a proteome-constrained optimisation problem with growth rate as
389 objective. Through our high resolution sampling around the critical dilution rate, we observed
390 distinct changes in proteins exactly at the onset of ethanol formation in the glucose-limited
391 chemostat. We also show that the active constraints that drive these changes can be different
392 under different conditions such as batch growth on galactose - even if ethanol is made in both
393 cases. Our approach to identify the active cellular constraints may resolve some of the
394 discussion in current literature about *the* cause of overflow metabolism, not only in yeast but
395 possibly also in other eukaryotes, including discussion about the Warburg effect in mammalian
396 cells⁴⁴.

397 Second, the proteome constraints of the model are currently based on experimental
398 observations, but further research could drill deeper into their origin. For example, why would
399 the protein density in the cytosol be relatively constant; Does this balance diffusion rates with
400 catalytic capacities⁴⁵? Are the current morphological dimensions of a yeast cell optimal for
401 growth rate? Recent work on selection for cell number showed that smaller cells can be readily
402 selected for⁴⁶. We also identified that the levels of glucose transport and that of mitochondria
403 need to be constrained to describe the data. Why would yeast not express these components at
404 higher levels? In the case of mitochondria, the proteomics data suggest that rather than a
405 maximum mitochondrial membrane area and matrix volume, there is a maximal rate of
406 mitochondrial biogenesis. Can we calculate this rate from first principles? One could imagine
407 that an upper limit for mitochondrial “growth rate” exists if all but eight metabolic proteins need
408 to be transported over the same membrane that must also harbour the full machinery for
409 oxidative phosphorylation. Moreover, we focused on mitochondrial protein content, and ignored
410 details on morphology, lipid synthesis, or possible assembly costs. Thus, a next version of the

411 model will need to address the mitochondrial transport, biosynthesis and morphology in much
412 more detail.

413 In the case of glucose transport, the model suggested that further increase in glucose
414 transporters beyond wild type expression did not increase growth rate substantially and would
415 likely be invisible for evolution. At maximal saturation of the transporter, glucose transport
416 expression was (just) no longer an active constraint in our model (Fig. 2e). Thus, it appears as if
417 yeast expresses just enough glucose transporters to maximise its growth rate under glucose
418 excess – as found in bacteria⁴⁷. Expressing higher transport levels at lower glucose levels would
419 enhance growth rate but may not pay off if this state is a transient towards glucose starvation, or
420 could be outright dangerous if suddenly glucose would become available³⁷. The expression level
421 of the hexose transporters may thus have evolved to be an adaptation to dynamic
422 environments⁴⁸. Long-term evolution experiments in glucose-limited chemostats indeed show
423 gene duplications of high-affinity glucose transporters⁴⁹, showing that growth limitation, and
424 hence selection pressure, is on glucose transport under these conditions.

425 Third, in the case of nutrient uptake limitation, there appears to be “excess” proteome
426 space that could be filled with anticipatory proteins or heterologous enzymes at no cost in
427 fitness. Even though the composition of such excess proteome space cannot be predicted with
428 our model, we were able to predict metabolic fluxes very well: in this nutrient-limited regime
429 metabolic efficiency (ATP per glucose), not proteome efficiency (ATP per protein), determines
430 the best growth rate strategy. This explains why Flux Balance Analysis applied to only the
431 metabolic network has been so successful, but only under nutrient-limited conditions.

432 Finally, we found linear or even proportional relationships between growth rate and
433 flux, and between flux and enzyme levels in a sugar excess (batch culture) regime. In terms of
434 regulation analysis⁵⁰, such a regime is characterised by hierarchical regulation with absence of
435 metabolic regulation, that is, all changes in flux are brought about by changes in enzyme levels,
436 not their degree of saturation. For glycolysis and amino acid metabolism, the average saturation,
437 estimated as the ratio of the predicted minimal enzyme level to the expressed enzyme level, at

438 maximal growth rate is around 0.5, incidently the level predicted as theoretical optimum for
439 specific reaction rate⁵¹. In contrast, when growth is limited by glucose availability, the degree of
440 saturation varies and the model suggests a mixture of hierarchical and metabolic regulation, as
441 previously observed in chemostats as well⁵².

442 To conclude, we present a mechanistic, compartmentalized, model of an eukaryal
443 organism in full details, which can act as a valuable, computable, knowledge base. We show how
444 it can be used to compute protein costs and identify active growth-limiting constraints, and how
445 it can be combined with quantitative flux and proteomics data to provide unprecedented insight
446 into cellular physiology. Finally, we show that also in eukaryal cells, metabolic strategies can be
447 understood on the basis of growth rate optimisation under nutrient and proteome constraints.
448 What remains to be understood is how the cell's signalling and regulatory networks manage to
449 implement these (optimal) proteome allocation strategies.

450

451 **Methods**

452 **Model development**

453 The full description of the pcYeast model is provided as Supplementary Notes. The model codes
454 are available per request to the authors and will be published on GitHub upon acceptance of this
455 manuscript.

456

457 **Strains and shake flask cultivation**

458 The strain used for this study was *Saccharomyces cerevisiae* strain CEN.PK 113-7D⁵³. The stocks
459 used for the experiments were grown in 500 mL shake flask containing 100 mL of YPD medium
460 (10 g L⁻¹ of Bacto yeast extract, 20 g L⁻¹ of peptone and 20 g L⁻¹ of D-glucose). The culture was
461 grown up to early stationary phase and 1 mL aliquots were stored in 20% (v/v) of glycerol at -
462 80 °C. For chemostats, pre-cultures were grown in 500 mL shake flasks containing 100 mL of
463 synthetic medium, the pH was set to 6.0 with 2M KOH and the medium was supplemented with

464 20 g L⁻¹ of D-glucose⁵⁴. Shake flasks with medium were inoculated with the 1 mL frozen stocks of
465 the strain and the cultivations were performed in an orbital shaker at 200 rpm at 30 °C. Pre-
466 cultures for batches with translation inhibitors were performed using a similar approach,
467 whereas for batches with different carbon sources the pre-cultures were made with the
468 respective carbon sources instead of D-glucose.

469

470 **Chemostat cultivations**

471 Chemostat cultivations were performed in 2 L bioreactors (Applikon, Schiedam, The
472 Netherlands) with a working volume of 1.0 L, the dilution rates used in this study were 0.2, 0.23,
473 0.27, 0.3, 0.32 and 0.34 h⁻¹ in two independent replicate cultures. Growth rates were controlled
474 by modifying the inflow rate on each experiment. Synthetic medium according to Verduyn⁵⁴
475 supplemented with 7.5 g L⁻¹ of glucose and 0.25 g L⁻¹ Pluronic 6100 PE antifoaming agent was
476 supplied to the bioreactor from a 20 L continuously mixed reservoir vessel. Cultures were
477 sparged with dried air at a flow rate of 700 mL min⁻¹ and stirred at 800 rpm. The pH of the
478 cultures was maintained at 5.0 by automatic addition of 2 M KOH. If, after at least six volume
479 changes, the cultures dry cell weight concentration and carbon dioxide production rate differed
480 less than 2% over two consecutive volume changes the cultures were considered to be in steady
481 state. For cultures with dilution rates of 0.27, 0.3, 0.32 and 0.34 h⁻¹, cultures were first
482 maintained at a dilution rate of 0.2 h⁻¹ for 15 hours (3 volume changes) prior to increasing the
483 specific dilution rate to said values.

484

485 **Batch cultivations with different carbon sources**

486 Batch cultivations were performed using synthetic medium⁵⁴, the medium was supplemented
487 with 20 g L⁻¹ final concentrations of the carbon sources, either D-trehalose, D-galactose, D-
488 maltose or D-glucose (Sigma Aldrich). The bioreactors were inoculated with 100 mL of yeast
489 shake flask cultures, exponentially growing on the specific carbon source. The final OD₆₆₀ of all
490 pre-cultures was 4. Cultivations were performed at 30 °C, the pH was kept at 5.0 by automatic

491 addition of 2M KOH. The working volume of the bioreactors was 1.4 L in 2 L bioreactors
492 (Applikon, Schiedam, The Netherlands). The cultures were stirred at 8000 rpm and sparged
493 with a flow rate of 700 mL min⁻¹ of dried air. Oxygen levels were kept above 40% of the initial
494 saturation level as measured with Clark electrode (Mettler Toledo, Greifensee, Switzerland).

495

496 **Batch cultivations with the translation inhibitor cycloheximide**

497 Batch cultivations with the translation inhibitor cycloheximide were performed as for the
498 batches with different carbon sources, except that all the batch cultures ran on 20 g L⁻¹ of D-
499 glucose and were supplemented with different concentrations of cycloheximide with the aim of
500 reaching specific growth rates. In total five growth rates were studied, being 0.06, 0.12, 0.2, 0.32
501 and 0.41 h⁻¹ (adding respective cycloheximide concentrations of 228.96, 124.51, 52.15, 25.99
502 and 0 µg L⁻¹).

503

504 **Analytical methods**

505 Cultures dry weight was measured by filtering 20 mL of culture, the sample was filtered in pre-
506 dried and pre-weight membrane filters with a pore size of 0.45 µm (Gelman Science), the filter
507 was washed with demineralized water, subsequently it was dried in a microwave (20 min, 350
508 W) and the final weight was measured as described previously.

509 For the measurement of organic acids and residual carbon source concentrations, supernatants
510 of the cultures were used. For carbon-limited chemostat cultures, the samples were directly
511 quenched with cold steel beads and filtered⁵⁵, whereas samples from batch cultures were
512 centrifuged (5 min at 16.000× *g*). The supernatants were analysed by high-performance
513 chromatography analysis on an Agilent 1100 HPLC (Agilent Technologies) equipped with an
514 Aminex HPX-87H ion-exchange column (BioRad, Veenendaal, The Netherlands), operated with 5
515 mM H₂SO₄ as the mobile phase at a flow rate of 0.6 mL min⁻¹ and at 60 °C. Detection was
516 according to a dual-wavelength absorbance detector (Agilent G1314A) and a refractive-index
517 detector (Agilent G1362A), as described previously.

518 The exhaust gas from batch cultures was cooled down with a condenser (2°C) and dried with a
519 PermaPure Dryer (model MD 110-8P-4; Inacom Instruments, Veenendaal, the Netherlands)
520 before online analysis of carbon dioxide and oxygen with a Rosemount NGA 2000 Analyser
521 (Baar, Switzerland).

522

523 **Glycogen and trehalose assays**

524 1 mL of culture was taken from the chemostats and directly added to 5 mL of cold methanol (-40
525 °C). The sample was mixed and centrifuged (4400× *g*, -20 °C for 5 minutes), the supernatant
526 was discarded, and the pellet was washed in 5 mL of cold methanol (-40 °C), and pellets were
527 stored at -80 °C until further processing. Subsequently, the pellets were resuspended in 0.25 M
528 Na₂CO₃ and processed as described previously^{56,57}. D-glucose released from trehalose and
529 glycogen were measured with a D-glucose assay kit (K-GLUC Megazyme), two biological
530 replicates and three technical replicates were analysed per condition.

531

532 **RNA determination**

533 For RNA determination, 1-2 mL of broth was transferred to a filter (pore size of 0.45 µm, Gelman
534 Science), after which the filter was washed with cold TCA 5 %. The cells were resuspended in 3
535 mL of TCA 5% and centrifuged for 15 minutes at 4 °C at 4000 rpm. The supernatant was
536 removed and the pellet was stored at -20 °C. Finally, samples were processed as described by
537 Popolo et al., 1982. Two biological replicates and three technical replicates were analysed per
538 condition.

539

540 **Protein determination**

541 For the batches with CHX, culture volumes corresponding to 50 mg of DCW were centrifuged,
542 washed twice with cold demineralized sterile water and divided into two aliquots of 5 mL. 2 mL
543 of the aliquot (containing 10 mg DW) was mixed with 1 mL of 3 M NaOH and incubated at 100 °C
544 for 10 minutes. The final mix was diluted and processed following the copper-sulfate based

545 method as described previously⁵⁸. The absorbance of the supernatant was measured at 510 nm,
546 for calibration lyophilized bovine serum albumin (A2153, Sigma Aldrich) was used. Two
547 biological replicates and 3 technical replicates were analysed per condition.

548

549 **Proteomics sample preprocessing**

550 Aliquots of 20 mL of culture from chemostats and batches with different carbon sources were
551 centrifuged (4000 rpm 4 °C, 10 minutes) and washed two times, the final pellet was flash frozen
552 in liquid nitrogen and stored at -80 °C. Two biological replicates and two technical replicates
553 were analysed per condition.

554 Frozen cell pellets were thawed on ice before transfer to Precellys[®] Lysing Kit 2 ml screw cap
555 vials with 0.5mm glass beads (Bertin Instruments, France). Lysis was performed in 250 µl lysis
556 buffer, 50 mM ammonium bicarbonate with cOmplete protease inhibitor cocktail (ROCHE,
557 Switzerland), using a Minilys Personal Tissue Homogenizer (Bertin Instruments, France), at
558 maximum speed for 15 cycles of 30 seconds with a one-minute rest on ice between each cycle.
559 Lysed material was centrifuged for 10 minutes 13,000× *g* at 4°C, the supernatant fraction was
560 removed and retained. Fresh lysis buffer (250 µl) was added to the insoluble material, which
561 was resuspended before extraction from the vial via a small hole inserted into the vial base.
562 Soluble and insoluble fractions were recombined and the total final volume recorded. Protein
563 concentration was determined using Pierce[™] Coomassie Plus Bradford Assay Kit (ThermoFisher
564 Scientific, UK).

565 Protein (100 µg) from each sample was treated with 0.05 % (w/v) RapiGest[™] SF surfactant
566 (Waters, UK) at 80 °C for 10 minutes, reduced with 4 mM dithiothreitol (Melford Laboratories
567 Ltd., UK) at 60 °C for 10 minutes and subsequently alkylated with 14 mM iodoacetamide
568 (SIGMA, UK) at room temperature for 30 minutes. Proteins were digested with 2 µg Trypsin
569 Gold, Mass Spectrometry Grade (Promega, US) at 37 °C for 4 hours before a top-up of a further 2
570 µg trypsin and incubation at 37 °C overnight. Digests were acidified by addition of trifluoroacetic
571 acid (Greyhound Chromatography and Allied Chemicals, UK) to a final concentration of 0.5 %

572 (v/v) and incubated at 37 °C for 45 minutes before centrifugation at 13,000× *g* (4°C) to remove
573 insoluble non-peptidic material.

574

575 **Proteomics analytics**

576 The sample running order was randomised using a random number generator (Random.org).

577 Samples were analysed using an UltiMate™ 3000 RSLCnano system (ThermoFisher Scientific)

578 coupled to a Q Exactive™ HF Hybrid Quadrupole-Orbitrap™ Mass Spectrometer. Protein digests

579 (1 ug of each) were loaded onto a trapping column (Acclaim PepMap 100 C18, 75 µm x 2 cm, 3

580 µm packing material, 100 Å) using 0.1 % (v/v) trifluoroacetic acid, 2 % (v/v) acetonitrile in

581 water at a flow rate of 12 µL min⁻¹ for 7 min.

582 The peptides were eluted onto the analytical column (EASY-Spray PepMap RSLC C18, 75 µm x

583 50 cm, 2 µm packing material, 100 Å) at 40°C using a linear gradient of 120 minute shallow

584 gradient rising from 8 % (v/v) acetonitrile/0.1 % (v/v) formic acid (Fisher Scientific, UK) to 30

585 % (v/v) acetonitrile/0.1 % (v/v) formic acid at a flow rate of 300 nL min⁻¹. The column was then

586 washed at 1 % A : 99 % B for 8 min, and re-equilibrated to starting conditions. The nano-liquid

587 chromatograph was operated under the control of Dionex Chromatography MS Link 2.14.

588 The nano-electrospray ionisation source was operated in positive polarity under the control of

589 QExactive HF Tune (version 2.5.0.2042), with a spray voltage of 2.1 kV and a capillary

590 temperature of 250°C. The mass spectrometer was operated in data-dependent acquisition

591 mode. Full MS survey scans between *m/z* 300-2000 were acquired at a mass resolution of

592 60,000 (full width at half maximum at *m/z* 200). For MS, the automatic gain control target was

593 set to 3e⁶, and the maximum injection time was 100 ms. The 16 most intense precursor ions

594 with charge states of 2-5 were selected for MS/MS with an isolation window of 2 *m/z* units.

595 Product ion spectra were recorded between *m/z* 200-2000 at a mass resolution of 30,000 (full

596 width at half maximum at *m/z* 200). For MS/MS, the automatic gain control target was set to

597 1e⁵, and the maximum injection time was 45 ms. Higher-energy collisional dissociation was

598 performed to fragment the selected precursor ions using a normalised collision energy of 30 %.

599 Dynamic exclusion was set to 30 s.

600

601 **Proteomics data analysis**

602 The resulting raw data files generated by XCalibur (version 3.1) were processed using MaxQuant

603 software (version 1.6.0.16)⁵⁹. The search parameters were set as follows: label free experiment

604 with default settings; cleaving enzyme trypsin with 2 missed cleavages; Orbitrap instrument

605 with default parameters; variable modifications: oxidation (M) and Acetyl (protein N-term); first

606 search as default; in global parameters, the software was directed to the FASTA file; for

607 advanced identification “Match between runs” was checked; for protein quantification we only

608 used unique, unmodified peptides. All other MaxQuant settings were kept as default. The false

609 discovery rate (FDR) for accepted peptide spectrum matches and protein matches was set to

610 1%. The CEN.PK113-7D Yeast FASTA file was downloaded from the *Saccharomyces* Genome

611 Database (SGD) ([https://downloads.yeastgenome.org/sequence/strains/CEN.PK/CEN.PK113-](https://downloads.yeastgenome.org/sequence/strains/CEN.PK/CEN.PK113-7D/CEN.PK113-7D_Delft_2012_AEHG00000000/)

612 [7D/CEN.PK113-7D_Delft_2012_AEHG00000000/](https://downloads.yeastgenome.org/sequence/strains/CEN.PK/CEN.PK113-7D/CEN.PK113-7D_Delft_2012_AEHG00000000/)).

613

614 The resulting MaxQuant output was then analysed using the MSstats package (version 3.5.6)⁶⁰

615 in the R environment (version 3.3.3) to obtain differential expression fold changes with

616 associated *p* values, along with normalized LFQ and intensity values as described previously⁶¹.

617

618 **Acknowledgements**

619 This work was supported by NWO (NWO ERA-IB-2, project No 053.80.722 to BT and PDL) and

620 Biotechnology and Biological Sciences Research Council (BB/M025748/1 to S. Hubbard,

621 BB/M025756/1 to RB). PG and BT also acknowledge support by Marie Skłodowska-Curie

622 Actions ITN “SynCrop” (grant agreement No 764591). We thank SURFsara for the HPC resources

623 through access to the Lisa Compute Cluster.

624 Author Contributions

625 Conceptualization, funding acquisition and supervision: BT, JN, PDL, RB, S. Hubbard;
626 experimental data collection: ARP, VH, S. Holman; experimental data analysis: ARP, PG, MGA,
627 MMMB; computational modeling: IEE, PG; formal analysis: IEE, PG, JvH, FJB, NS, JN, PDL, BT;
628 writing – original draft: BT; writing – editing: IEE, PG, FJB, JN, BT. All authors have read and
629 approved the manuscript.

630

631 References

- 632 1. Blank, L., Lehmbeck, F. & Sauer, U. Metabolic-flux and network analysis in fourteen
633 hemiascomycetous yeasts. *FEMS Yeast Res.* **5**, 545–558 (2005).
- 634 2. Pfeiffer, T. & Morley, A. An evolutionary perspective on the Crabtree effect. *Front. Mol.*
635 *Biosci.* **1**, 1–6 (2014).
- 636 3. De Deken, R. H. The Crabtree effect: a regulatory system in yeast. *J. Gen. Microbiol.* **44**, 149–
637 156 (1966).
- 638 4. Van Hoek, P., Van Dijken, J. P. & Pronk, J. T. Effect of specific growth rate on fermentative
639 capacity of baker's yeast. *Appl. Environ. Microbiol.* **64**, 4226–4233 (1998).
- 640 5. de Groot, D. H., van Boxtel, C., Planqué, R., Bruggeman, F. J. & Teusink, B. The number of
641 active metabolic pathways is bounded by the number of cellular constraints at maximal
642 metabolic rates. *PLoS Comput. Biol.* **15**, e1006858 (2019).
- 643 6. Basan, M. *et al.* Overflow metabolism in Escherichia coli results from efficient proteome
644 allocation. *Nature* **528**, 99–104 (2015).
- 645 7. Molenaar, D., van Berlo, R., de Ridder, D. & Teusink, B. Shifts in growth strategies reflect
646 tradeoffs in cellular economics. *Mol. Syst. Biol.* **5**, 323 (2009).
- 647 8. Mori, M., Hwa, T., Martin, O. C., De Martino, A. & Marinari, E. Constrained Allocation Flux
648 Balance Analysis. *PLoS Comput. Biol.* **12**, 1–24 (2016).

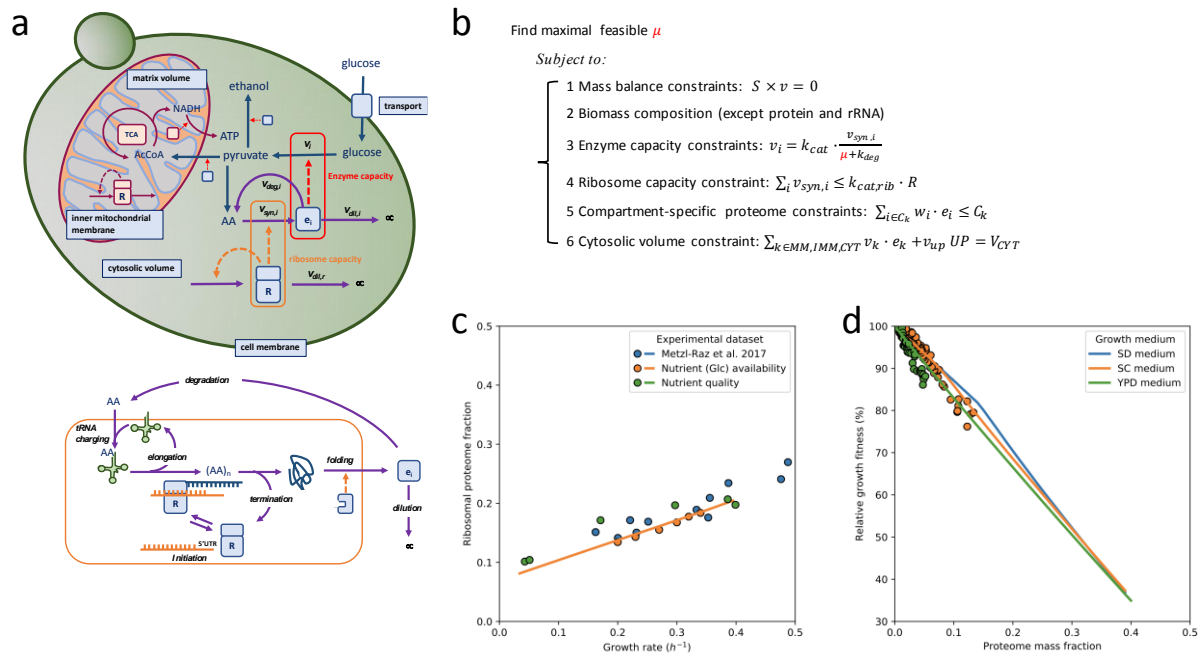
- 649 9. O'Brien, E. J., Lerman, J. A., Chang, R. L., Hyduke, D. R. & Palsson, B. Genome-scale models of
650 metabolism and gene expression extend and refine growth phenotype prediction. *Mol. Syst.*
651 *Biol.* **9**, (2013).
- 652 10. Scott, M., Gunderson, C. W., Mateescu, E. M., Zhang, Z. & Hwa, T. Interdependence of Cell
653 Growth and Gene Expression: Origins and Consequences. *Science* **330**, 1099–1102 (2010).
- 654 11. Wortel, M. T., Bosdriesz, E., Teusink, B. & Bruggeman, F. J. Evolutionary pressures on
655 microbial metabolic strategies in the chemostat. *Sci. Rep.* **6**, 29503 (2016).
- 656 12. Scott, M. & Hwa, T. Bacterial growth laws and their applications. *Curr. Opin. Biotechnol.* **22**,
657 559–565 (2011).
- 658 13. Wortel, M. T., Peters, H., Hulshof, J., Teusink, B. & Bruggeman, F. J. Metabolic states with
659 maximal specific rate carry flux through an elementary flux mode. *FEBS J.* **281**, 1547–1555
660 (2014).
- 661 14. Berkhout, J. *et al.* How biochemical constraints of cellular growth shape evolutionary
662 adaptations in metabolism. *Genetics* **194**, 505–512 (2013).
- 663 15. Bosdriesz, E., Molenaar, D., Teusink, B. & Bruggeman, F. J. How fast-growing bacteria
664 robustly tune their ribosome concentration to approximate growth-rate maximization. *FEBS*
665 *J.* **282**, 2029–2044 (2015).
- 666 16. Metzl-Raz, E. *et al.* Principles of cellular resource allocation revealed by condition-dependent
667 proteome profiling. *eLife* **6**, e28034 (2017).
- 668 17. Sánchez, B. J. *et al.* Improving the phenotype predictions of a yeast genome-scale metabolic
669 model by incorporating enzymatic constraints. *Mol. Syst. Biol.* **13**, 935 (2017).
- 670 18. Björkeröth, J. *et al.* Proteome reallocation from amino acid biosynthesis to ribosomes
671 enables yeast to grow faster in rich media. *Proc. Natl. Acad. Sci.* **117**, 21804–21812 (2020).
- 672 19. Sánchez, B. J., Feiran Li, Hongzhong Lu, Kerkhoven, E. & Nielsen, J. *SysBioChalmers/yeast-*
673 *GEM: yeast 7.6.0*. (Zenodo, 2016). doi:10.5281/ZENODO.1495468.

- 674 20. Beg, Q. K. *et al.* Intracellular crowding defines the mode and sequence of substrate uptake by
675 *Escherichia coli* and constrains its metabolic activity. *Proc. Natl. Acad. Sci.* **104**, 12663–
676 12668 (2007).
- 677 21. Adadi, R., Volkmer, B., Milo, R., Heinemann, M. & Shlomi, T. Prediction of microbial growth
678 rate versus biomass yield by a metabolic network with kinetic parameters. *PLoS Comput.*
679 *Biol.* **8**, (2012).
- 680 22. Labhsetwar, P. *et al.* Population FBA predicts metabolic phenotypes in yeast. *PLOS Comput.*
681 *Biol.* **13**, e1005728 (2017).
- 682 23. Nilsson, A. & Nielsen, J. Metabolic Trade-offs in Yeast are Caused by F1F0-ATP synthase. *Sci.*
683 *Rep.* **6**, 22264 (2016).
- 684 24. Zhuang, K., Vemuri, G. N. & Mahadevan, R. Economics of membrane occupancy and respiro-
685 fermentation. *Mol. Syst. Biol.* **7**, 1–9 (2011).
- 686 25. Okamoto, K. The protein import motor of mitochondria: a targeted molecular ratchet driving
687 unfolding and translocation. *EMBO J.* **21**, 3659–3671 (2002).
- 688 26. Kafri, M., Metzler-Raz, E., Jona, G. & Barkai, N. The Cost of Protein Production. *Cell Rep.* **14**, 22–
689 31 (2016).
- 690 27. Bruggeman, F. J., Planqué, R., Molenaar, D. & Teusink, B. Searching for principles of microbial
691 physiology. *FEMS Microbiol. Rev.* **44**, 821–844 (2020).
- 692 28. Famili, I., Forster, J., Nielsen, J. & Palsson, B. O. *Saccharomyces cerevisiae* phenotypes can be
693 predicted by using constraint-based analysis of a genome-scale reconstructed metabolic
694 network. *Proc. Natl. Acad. Sci.* **100**, 13134–13139 (2003).
- 695 29. Canelas, A. B., Ras, C., ten Pierick, A., van Gulik, W. M. & Heijnen, J. J. An in vivo data-driven
696 framework for classification and quantification of enzyme kinetics and determination of
697 apparent thermodynamic data. *Metab. Eng.* **13**, 294–306 (2011).
- 698 30. Jules, M., Guillou, V., François, J. & Parrou, J.-L. Two distinct pathways for trehalose
699 assimilation in the yeast *Saccharomyces cerevisiae*. *Appl. Environ. Microbiol.* **70**, 2771–2778
700 (2004).

- 701 31. Diderich, J. A. *et al.* Glucose uptake kinetics and transcription of HXT genes in chemostat
702 cultures of *Saccharomyces cerevisiae*. *J. Biol. Chem.* **274**, 15350–15359 (1999).
- 703 32. Teusink, B., Diderich, J. A., Westerhoff, H. V., van Dam, K. & Walsh, M. C. Intracellular Glucose
704 Concentration in Derepressed Yeast Cells Consuming Glucose Is High Enough To Reduce the
705 Glucose Transport Rate by 50%. *J. Bacteriol.* **180**, 556–562 (1998).
- 706 33. Chen, Y. & Nielsen, J. Energy metabolism controls phenotypes by protein efficiency and
707 allocation. *Proc. Natl. Acad. Sci.* **116**, 17592–17597 (2019).
- 708 34. O'Brien, E. J., Utrilla, J. & Palsson, B. O. Quantification and Classification of *E. coli* Proteome
709 Utilization and Unused Protein Costs across Environments. *PLoS Comput. Biol.* **12**,
710 e1004998 (2016).
- 711 35. Goel, A. *et al.* Protein costs do not explain evolution of metabolic strategies and regulation of
712 ribosomal content: does protein investment explain an anaerobic bacterial Crabtree effect?:
713 Protein costs and evolution of metabolic strategies. *Mol. Microbiol.* **97**, 77–92 (2015).
- 714 36. de Jongh, W. A. *et al.* The roles of galactitol, galactose-1-phosphate, and phosphoglucomutase
715 in galactose-induced toxicity in *Saccharomyces cerevisiae*. *Biotechnol. Bioeng.* **101**, 317–326
716 (2008).
- 717 37. Postma, E., Verduyn, C., Kuiper, A., Scheffers, W. A. & Van Dijken, J. P. Substrate-accelerated
718 death of *Saccharomyces cerevisiae* CBS 8066 under maltose stress. *Yeast* **6**, 149–158 (1990).
- 719 38. Hong, K.-K., Vongsangnak, W., Vemuri, G. N. & Nielsen, J. Unravelling evolutionary strategies
720 of yeast for improving galactose utilization through integrated systems level analysis. *Proc.*
721 *Natl. Acad. Sci. U. S. A.* **108**, 12179–12184 (2011).
- 722 39. Keren, L. *et al.* Massively Parallel Interrogation of the Effects of Gene Expression Levels on
723 Fitness. *Cell* **166**, 1282–1294.e18 (2016).
- 724 40. Chaker-Margot, M. Assembly of the small ribosomal subunit in yeast: mechanism and
725 regulation. *RNA* **24**, 881–891 (2018).
- 726 41. Kunkel, J., Luo, X. & Capaldi, A. P. Integrated TORC1 and PKA signaling control the temporal
727 activation of glucose-induced gene expression in yeast. *Nat. Commun.* **10**, 3558 (2019).

- 728 42. Chubukov, V., Gerosa, L., Kochanowski, K. & Sauer, U. Coordination of microbial metabolism.
729 *Nat. Rev. Microbiol.* **12**, 327–340 (2014).
- 730 43. Hofmeyr, J. S. & Cornish-Bowden, A. Regulating the cellular economy of supply and demand.
731 *FEBS Lett.* **476**, 47–51 (2000).
- 732 44. Vander Heiden, M. G. & DeBerardinis, R. J. Understanding the Intersections between
733 Metabolism and Cancer Biology. *Cell* **168**, 657–669 (2017).
- 734 45. Dill, K. A., Ghosh, K. & Schmit, J. D. Physical limits of cells and proteomes. *Proc. Natl. Acad. Sci.*
735 **108**, 17876–17882 (2011).
- 736 46. van Tatenhove-Pel, R. J. *et al.* Serial propagation in water-in-oil emulsions selects for
737 *Saccharomyces cerevisiae* strains with a reduced cell size or an increased biomass yield on
738 glucose. *Metab. Eng.* **64**, 1–14 (2021).
- 739 47. Jensen, P. R., Michelsen, O. & Westerhoff, H. V. Control analysis of the dependence of
740 *Escherichia coli* physiology on the H(+)-ATPase. *Proc. Natl. Acad. Sci.* **90**, 8068–8072
741 (1993).
- 742 48. Buziol, S. *et al.* Dynamic response of the expression of hxt1, hxt5 and hxt7 transport proteins
743 in *Saccharomyces cerevisiae* to perturbations in the extracellular glucose concentration. *J.*
744 *Biotechnol.* **134**, 203–210 (2008).
- 745 49. Gresham, D. *et al.* The Repertoire and Dynamics of Evolutionary Adaptations to Controlled
746 Nutrient-Limited Environments in Yeast. *PLoS Genet.* **4**, e1000303 (2008).
- 747 50. ter Kuile, B. H. & Westerhoff, H. V. Transcriptome meets metabolome: hierarchical and
748 metabolic regulation of the glycolytic pathway. *FEBS Lett.* **500**, 169–171 (2001).
- 749 51. Cornish-Bowden, A. The effect of natural selection on enzymic catalysis. *J. Mol. Biol.* **101**, 1–9
750 (1976).
- 751 52. Daran-Lapujade, P. *et al.* The fluxes through glycolytic enzymes in *Saccharomyces cerevisiae*
752 are predominantly regulated at posttranscriptional levels. *Proc. Natl. Acad. Sci.* **104**, 15753–
753 15758 (2007).

- 754 53. Nijkamp, J. F. *et al.* De novo sequencing, assembly and analysis of the genome of the
755 laboratory strain *Saccharomyces cerevisiae* CEN.PK113-7D, a model for modern industrial
756 biotechnology. *Microb. Cell Factories* **11**, 36 (2012).
- 757 54. Verduyn, C., Postma, E., Scheffers, W. A. & Van Dijken, J. P. Effect of benzoic acid on metabolic
758 fluxes in yeasts: A continuous-culture study on the regulation of respiration and alcoholic
759 fermentation. *Yeast* **8**, 501–517 (1992).
- 760 55. Mashego, M. R., van Gulik, W. M., Vinke, J. L. & Heijnen, J. J. Critical evaluation of sampling
761 techniques for residual glucose determination in carbon-limited chemostat culture
762 of *Saccharomyces cerevisiae*. *Biotechnol. Bioeng.* **83**, 395–399 (2003).
- 763 56. Parrou, J. L., Teste, M.-A. & François, J. Effects of various types of stress on the metabolism of
764 reserve carbohydrates in *Saccharomyces cerevisiae*: genetic evidence for a stress-induced
765 recycling of glycogen and trehalose. *Microbiology* **143**, 1891–1900 (1997).
- 766 57. Boer, V., Daran, J., Almering, M., Dewinde, J. & Pronk, J. Contribution of the transcriptional
767 regulator Leu3p to physiology and gene expression in nitrogen- and carbon-limited
768 chemostat cultures. *FEMS Yeast Res.* **5**, 885–897 (2005).
- 769 58. Verduyn, C., Postma, E., Scheffers, W. A. & van Dijken, J. P. Physiology of *Saccharomyces*
770 *Cerevisiae* in Anaerobic Glucose-Limited Chemostat Cultures. *J. Gen. Microbiol.* **136**, 395–
771 403 (1990).
- 772 59. Tyanova, S., Temu, T. & Cox, J. The MaxQuant computational platform for mass
773 spectrometry-based shotgun proteomics. *Nat. Protoc.* **11**, 2301–2319 (2016).
- 774 60. Choi, M. *et al.* MSstats: an R package for statistical analysis of quantitative mass
775 spectrometry-based proteomic experiments. *Bioinformatics* **30**, 2524–2526 (2014).
- 776 61. Garcia-Albornoz, M. *et al.* A proteome-integrated, carbon source dependent genetic
777 regulatory network in *Saccharomyces cerevisiae*. *Mol. Omics* **16**, 59–72 (2020).
- 778



779

780 **Fig. 1 pcYeast model formulation and calibration of protein synthesis parameters. a.** A schematic

781 overview of reactions in the model, their interdependence and constraints. Metabolic reactions v_i are
 782 proportional to enzyme concentrations e_i that are synthesized at rate $v_{syn,i}$ by the ribosomes R . Each
 783 protein can be degraded with rate $v_{deg,i} = k_{deg} \cdot e_i$ or diluted by growth rate $v_{dil,i} = \mu \cdot e_i$.

784 Compartment-specific constraints are indicated in the light-blue boxes. **b.** Optimisation problem with

785 the key constraints, including 1) steady-state mass balances; 2) production of biomass components

786 such as DNA, lipids, cell wall and polysaccharides. Proteins and tRNA are excluded as their synthesis

787 rates are optimisation variables 3) enzyme capacity constraints that couple metabolic flux to catalytic

788 rate $k_{cat,i}$, and the enzyme level, whose value at steady state is determined by its synthesis rate, rates

789 of enzyme degradation, and dilution by growth. Note we use equalities and hence enzymes work at

790 their maximal rate and minimal required protein levels are computed; 4) ribosome capacity that

791 defines an upper bound for protein synthesis rate; 5) compartment-specific proteome constraints that

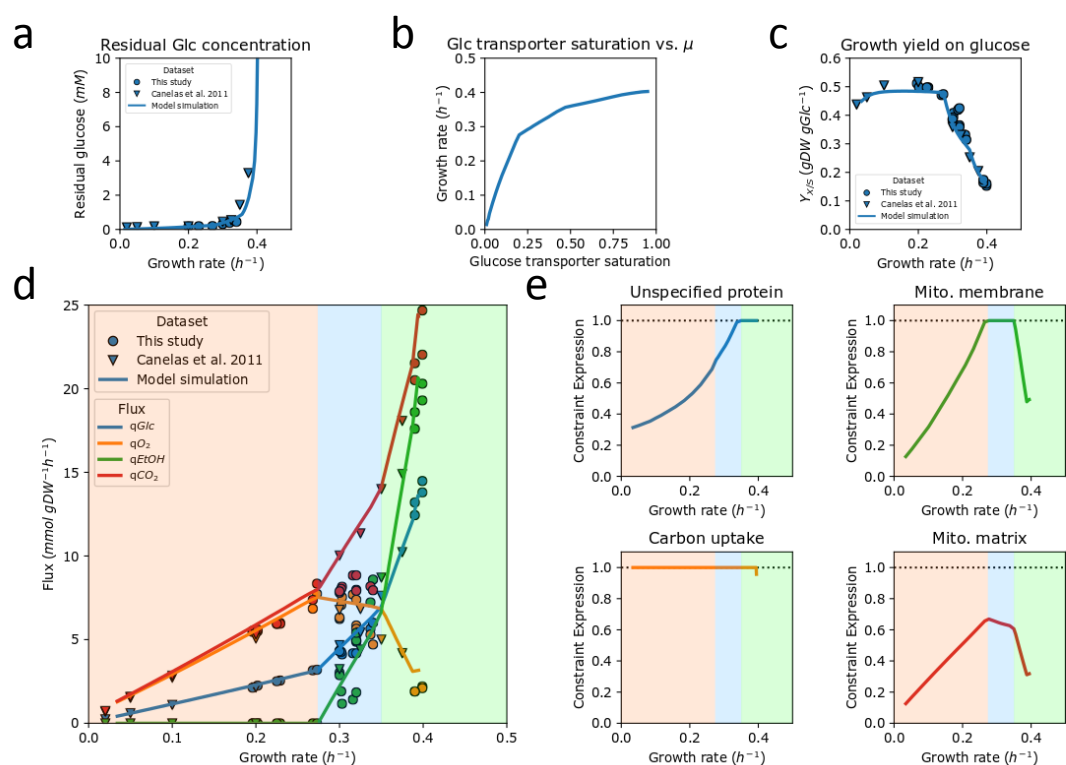
792 define the maximal concentration of proteins that can be contained in that compartment, with w_i the

793 specific volume or area of protein i ; 6) a cytosolic protein density constraint that has the same

794 function as that of proteome constraints, but whose equality forces the cell to fill up any vacant

795 proteome space with unspecified protein UP with average amino acid composition. **c.** Growth rate was

796 varied through sugar type (trehalose, galactose, maltose, glucose) or glucose concentration, and
797 ribosomal protein fraction was determined by proteomics (which was consistent with literature data,
798 also plotted). The translation rate was calibrated on that data, as detailed in **Supplementary Notes. d.**
799 Impact of mCherry protein overexpression on growth rate. Symbols show experimental data²⁶, solid
800 lines show model predictions based on glucose minimal (SD) medium or rich SC/YPD media.
801



802

803 **Fig. 2 Predicted and measured physiological response of *S. cerevisiae* CEN.PK as a function of glucose**

804 **availability a.** Measured (symbols) and predicted (line) residual glucose concentrations as a function of

805 growth rate. The latter was calculated based on published affinity for glucose and assuming negligible

806 intracellular glucose under these conditions. **b.** Maximal feasible growth rates of the model as a

807 function of the glucose transporter saturation. **c.** measured (symbols) and predicted biomass yield on

808 glucose. **d.** Experimental fluxes from glucose-limited chemostats at different dilution rates (circles) and

809 from two batch experiments (triangles): excess trehalose (which mimicks glucose limitation at low

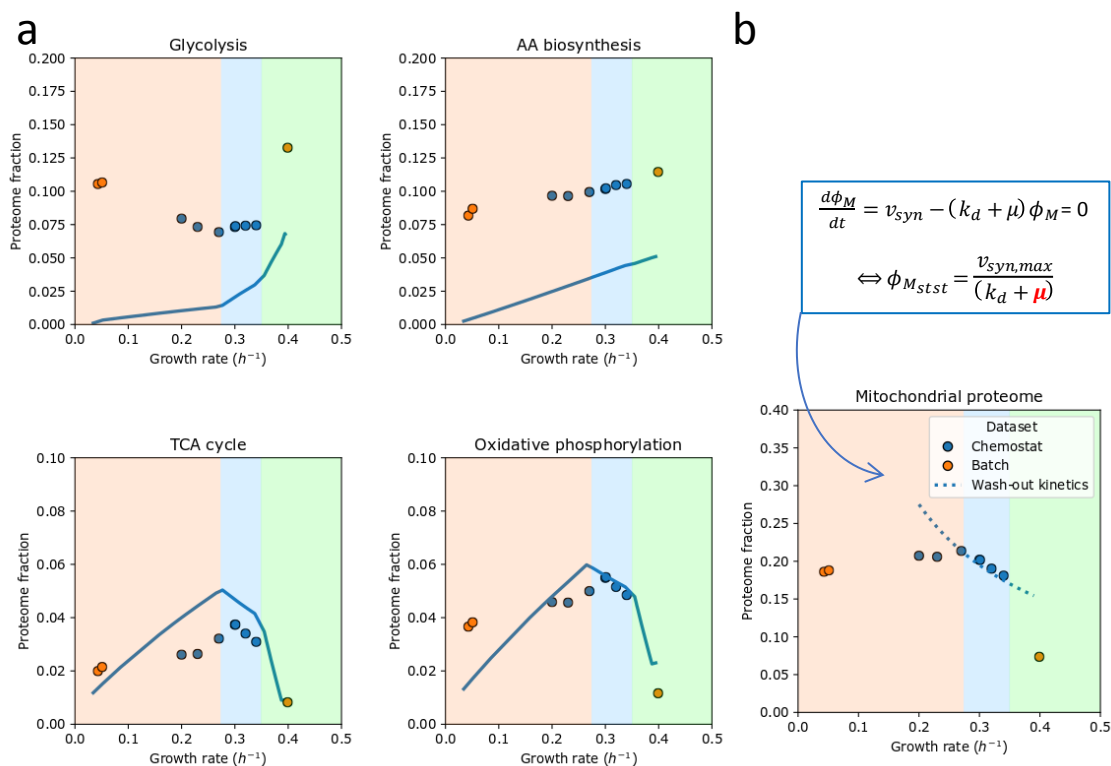
810 dilution rate³⁰) and excess glucose at the highest growth rate. The lines are model predictions;

811 background colors indicate regimes with different active constraints; **e.** Computed proteome

812 occupancy of different constrained protein pools. A fraction of 1 means that the compartment is full

813 with metabolically actively proteins and constrains the growth rate at that condition.

814



815

816 **Fig. 3 Proteomics data of selected pathways as a function of glucose availability.** Blue symbols are

817 glucose-limited chemostat data; orange symbols are controlled batch experiments with excess

818 trehalose (lowest growth rate) or glucose (highest growth rate) **a.** Comparison of predicted minimal

819 proteome fractions to sustain growth with the experimentally determined proteome fraction for four

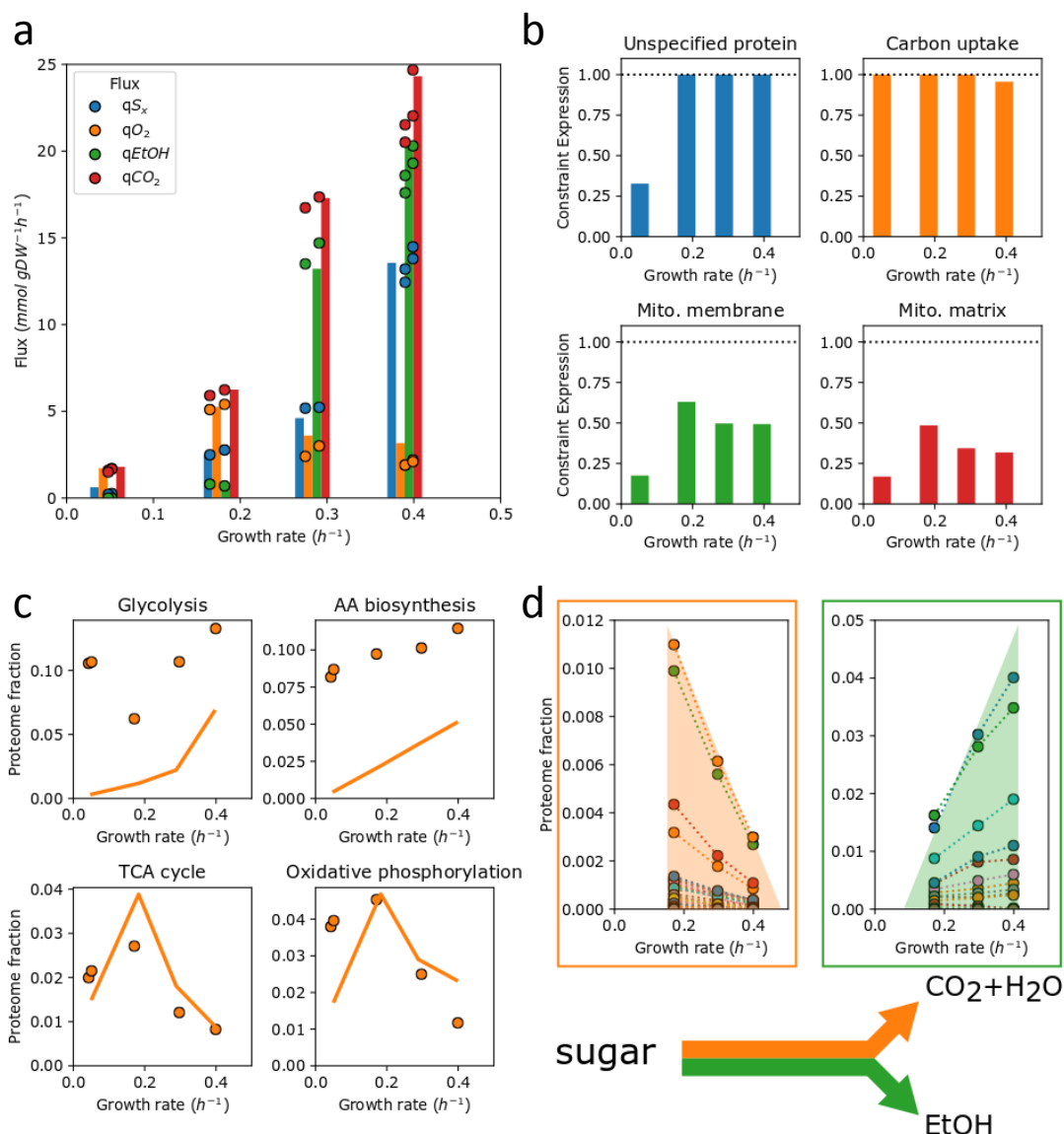
820 pathways. The ratio between the two represents an estimate of the saturation level of the constituent

821 enzymes. Lines represent the model; experimental data are symbols. **b.** Decay of steady-state

822 mitochondrial protein fraction with growth rate at onset of ethanol formation suggests a maximal rate

823 of mitochondrial biosynthesis $v_{syn,max}$.

824



825

826 **Fig. 4 Model predictions, fluxes and protein levels plotted as a function of growth rate during hexose**

827 **sugar excess conditions (in the order: trehalose, galactose, maltose, glucose) a. Fluxes of sugar**

828 **consumption, oxygen consumption and ethanol production. Circles are experimental data, bar plots**

829 **indicate model predictions (of both the growth rate and fluxes); b. Predicted active constraints under**

830 **the different sugar excess conditions as predicted by the mode (see legend of Fig. 2 for details). c.**

831 **Comparison of predicted minimally needed proteome fractions with experimentally determined ones**

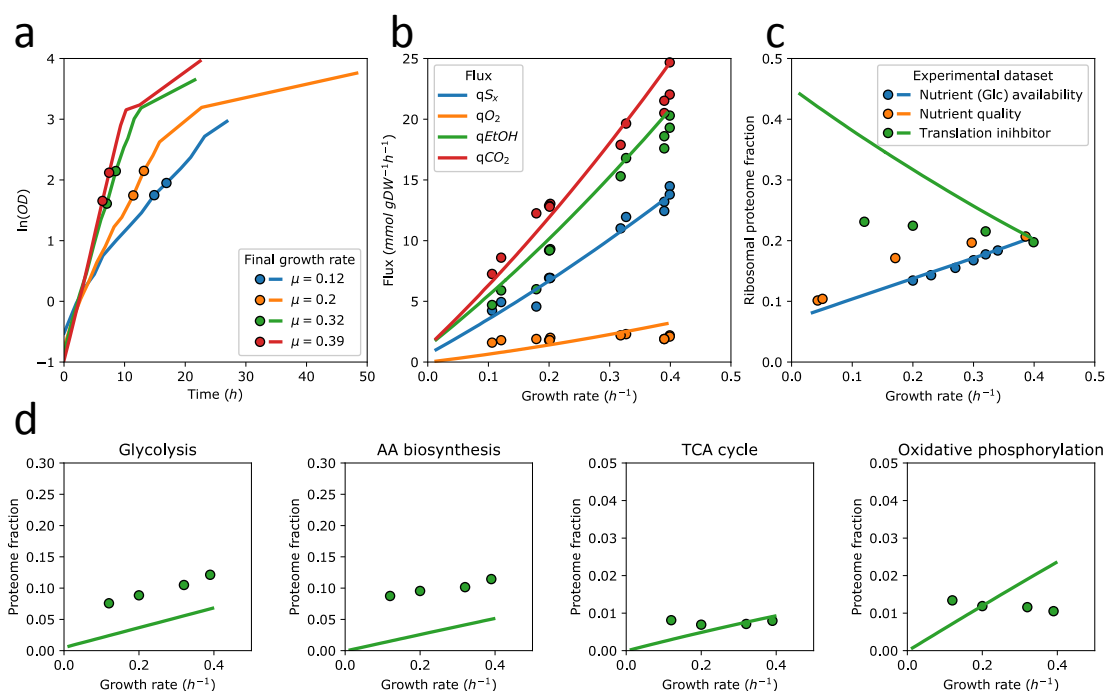
832 **suggests differences in saturation level between pathways. Lines represent the model, experimental**

833 **data are circles; d. Linearity of the expression of individual enzymes in glycolysis (right) and respiration**

834 (left) with growth rate suggests trading in of respiratory protein for fermentative protein. The

835 respiratory proteins converge at $0.474 \pm 0.0002 \text{ h}^{-1}$.

836



837

838 **Fig. 5 The effect of translation inhibition by cyclohexamide on growth rate, fluxes and proteome**

839 **fractions in controlled aerobic batch fermentations on glucose. a.** Dependency of culture optical density

840 (OD) on the time post-inoculation to the medium supplemented with cycloheximide. Lines are values

841 of consecutive OD measurements, points represent the times when cultures were sampled. **b.** Main

842 catabolic fluxes as a function of the growth rate. **c.** Ribosomal proteome fractions. Data from Fig. 1c

843 are included for comparison. **d.** Proteome fractions measured for key metabolic pathways, and the

844 minimal proteome fractions predicted by pcYeast. For b-d, lines are model predictions; symbols are

845 experimental data points.

846

847 **Table 1.** Statistics of the pcYeast model.

| Process/Compartment | # of reactions | # of proteins |
|---|-----------------------|----------------------|
| Total | 24422 | 1520 |
| Metabolic network | 5774 | 913 |
| from Yeast7.6 | 5738 | 909 |
| manually added metabolic reactions | 36 | 4 |
| Cytoplasm | 2349 | 778 |
| Plasma membrane | 529 | 114 |
| Mitochondria | 1089 | 272 |
| Endomembrane system | 2127 | 133 |
| Metabolic complex formation, disassembly, dilution | 2787 | - |
| tRNA turnover and modification | 2194 | 56 |
| Protein synthesis and turnover | 13312 | 403 |
| Cytoplasmic translation | 1512 | 138 |
| Mitochondrial translation | 8 | 89 |
| Protein folding | 1515 | 31 |
| Protein degradation | 1607 | 42 |
| Protein misfolding, refolding | 6061 | 73 |
| Protein transport | 1324 | 30 |
| Protein dilution by growth | 1285 | - |
| Formation of macromolecular complexes | 355 | 196 |

848

849 **Table 2.** Changes to the parameters for simulating sugar excess conditions. NGAM is non-growth
850 related ATP maintenance.

| Growth condition | Unit | Glucose (naïve) | Galactose | Maltose |
|---------------------------------|-----------------------------------|-----------------|-----------|---------|
| Maximal hexose transporter area | $\mu\text{m}^2/\text{cell}$ | 7.5 | 3.0 | 3.5 |
| Carbon-related NGAM | $\text{mmol}/\text{gDW}/\text{h}$ | 0.0 | 3.0 | 0.0 |
| Minimal UP fraction | $\text{g UP}/\text{g protein}$ | 0.245 | 0.49 | 0.34 |

851